A comparison of remote vs. local influence of El Niño on the coastal circulation of the northeast Pacific

Albert J. Hermann [a,*], Enrique N. Curchitser [b], Dale B. Haidvogel [c], Elizabeth L. Dobbins [a]

[a] *Joint Institute for the Study of the Atmosphere and Ocean, University of Washington, P.O. Box 357941, Seattle, WA 98195, USA*
[b] *Lamont-Doherty Earth Observatory of Columbia University, P.O. Box 1000, 61 Route 9W, Palisades, NY 10964-8000, USA*
[c] *Institute of Marine and Coastal Sciences, Rutgers University, 71 Dudley Road, New Brunswick, NJ 08901-8521, USA*

ABSTRACT

A set of spatially nested circulation models is used to explore interannual change in the northeast Pacific (NEP) during 1997–2002, and remote vs. local influence of the 1997–1998 El Niño on this region. Our nested set is based on the primitive equations of motion, and includes a basin-scale model of the north Pacific at ~40-km resolution (NPac), and a regional model of the Northeast Pacific at ~10-km resolution. The NEP model spans an area from Baja California through the Bering Sea, from the coast to ~2000-km offshore. In this context, "remote influence" refers to effects driven by changes in ocean velocity and temperature outside of the NEP domain; "local influence" refers to direct forcing by winds and runoff within the NEP domain. A base run of this model using hindcast winds and runoff for 1996–2002 replicates the dominant spatial modes of sea-surface height anomalies from satellite data, and coastal sea level from tide gauges. We have performed a series of sensitivity runs with the NEP model for 1997–1998, which analyze the response of coastal sea level to: (1) hindcast winds and coastal runoff, as compared to their monthly climatologies and (2) hindcast boundary conditions (from the NPac model), as compared to their monthly climatologies. Results indicate penetration of sea-surface height (SSH) from the basin-scale model into the NEP domain (e.g., remote influence), with propagation as coastal trapped waves from Baja up through Alaska. Most of the coastal sea-level anomaly off Alaska in El Niño years appears due to direct forcing by local winds and runoff (local influence), and such anomalies are much stronger than those produced off California. We quantify these effects as a function of distance along the coastline, and consider how they might impact the coastal ecosystems of the NEP.

© 2009 Elsevier Ltd. All rights reserved.

1. Introduction

Current systems of the northeast Pacific (hereafter referred to as "NEP") include Eastern Boundary Currents beyond narrow shelves of the West Coast of North America (the Alaska Current and California Current), and a Western Boundary Current along the shelf break south of Alaska (the Alaskan Stream). These form the outer rim of strong subtropical and subarctic gyres, which are set up by gyre-scale wind-stress curl and the resulting oceanic pressure fields. Closer to shore, the near-coastal wind stress and coastal runoff are predominant forces driving the ocean circulation. It has long been recognized that coastal trapped waves (CTWs) explain much of the variance in currents along the coast from California through British Columbia (Enfield and Allen, 1980); the impact of CTWs in the Coastal Gulf of Alaska (CGOA) region has been more controversial. In particular, it has been

suggested that scattering by irregular shelf topography near the shelf break (that is, canyons of many sizes) precludes the effective propagation of CTWs in the CGOA. Over a sufficiently broad shelf, the impact of such canyons may be reduced to such an extent that near-coastal signals propagate unhindered; however, the increased width of the shelf in the CGOA may itself steer remotely generated CTWs offshore. Hickey (1997) and Strub and James (2002a–c) have summarized the large-scale dynamics of these coastal systems. Important features include the seasonal evolution of the alongshore pressure gradient.

These factors are relevant not only to the seasonal cycle of sea-surface height (SSH) and currents in the NEP, but also to their response to El Niño and other large-scale climate variations. Roughly speaking, physical changes to the NEP may be driven in two ways: (1) "local" forcing from the overlying atmosphere and coastal runoff, e.g., through teleconnected changes in local winds, heat fluxes and precipitation associated with El Niño; (2) "remote" forcing, which enters through the western and southern boundaries of the NEP. The latter includes both the rapid communication of anomalous SSH and temperature signals

* Corresponding author.
 E-mail address: Albert.J.Hermann@noaa.gov (A.J. Hermann).

through waves (and CTWs in particular), and the slower direct advection of anomalous T and S fields into the NEP domain from the larger north Pacific (NPac).

A large number of studies have considered the problem of remote and local forcing of the NEP generally, and by El Niño in particular. Emery and Hamilton (1985) found that ENSO was associated with NPac SLP patterns, which promote higher SST and SSH along the coast. Pares-Sierra and O'Brien (1989) used a reduced-gravity model to study remote vs. local effects on the California Current system; they concluded that the interannual variability of coastal sea level (CSL) was primarily remotely forced by coastally trapped Kelvin waves. Johnson and O'Brien (1990) used primitive equation models to investigate El Niño-related forcing of the thermocline in the NEP. They concluded that near-coastal variations off Washington and Oregon were strongly driven by the large-scale atmospheric conditions, whereas to the south they were strongly driven by equatorial Kelvin waves. Meyers et al. (1996) looked at interdecadal variability of the NEP with a reduced-gravity model, and explored the impact of basin Rossby waves forced by the remotely generated coastal Kelvin waves. Strub and James (2002a–c) used SSH, SLP and SST data to diagnose remote vs. local effects of the 1997–1998 El Niño along the coast. They verified the importance of both remote and local effects, with a predominance of the former between the equator and the Gulf of California, and predominance of the latter between the Pacific Northwest and the Gulf of Alaska.

The purpose of this paper is twofold: first, to describe a NEP circulation model being used for biophysical investigations under US GLOBEC; second, to describe model experiments used to assess the relative importance of remote and local forcing effects on the NEP. Note that the chosen domain size should strongly affect the relative importance of forcing effects; our definition of "remote" and "local" is based on the placement of an arbitrary boundary between what we define as "the NEP" and the rest of the world. Indeed, if we draw such a boundary around a small enough patch of the real ocean, "remote" forcing will predominate, and with a large enough area (the entire globe) all forcing is by definition "local". For this study, we define "local" as within ~2000 km from the coast, between the Baja Peninsula and the Bering Sea (Fig. 1); all the rest of the world ocean is then by definition "remote".

A similar, model-based approach to the problem of local vs. remote forcing of the NEP was carried out by Melsom et al. (2003; hereafter referred to as MMH03), utilizing an isopycnal model of the full Pacific Basin. The present study differs from theirs in several respects. The MMH03 model covered the full Pacific Basin but with no coastal bathymetry or coastal runoff; in our study a smaller regional model was used, with bathymetry and runoff effects included. In MMH03, remote equatorial effects were removed by masking out the equatorial region from the basin model, and modifying the equatorial winds (which they derived from a hybrid of Hellerman and Rosenstein, 1983 and ECMWF, 1995), so as to minimize the creation of Kelvin waves near the equator. Here, we selectively retain daily hindcast boundary forcing from a basin-scale model (NPac, described in Curchitser et al., 2005), or replace it with a monthly climatology prepared from that model.

Throughout this paper we refer to the effect of remote and local forcing on both sea-surface height anomalies (SSHAs) near the shelf, and on coastal sea level specifically. The cross-shelf location of the CTW waveguide, and the forcing and expression of CTWs at the coast proper, both depend on many factors (e.g., slope, stratification, shelf width and latitude). In this paper we do not attempt to quantify the cross-shelf gradient of the CTW signal at any location. We do assume in our analysis that the waveguide is roughly parallel to the coast, and that CTWs are expressed to varying degrees in both SSHA and CSL. This expression will
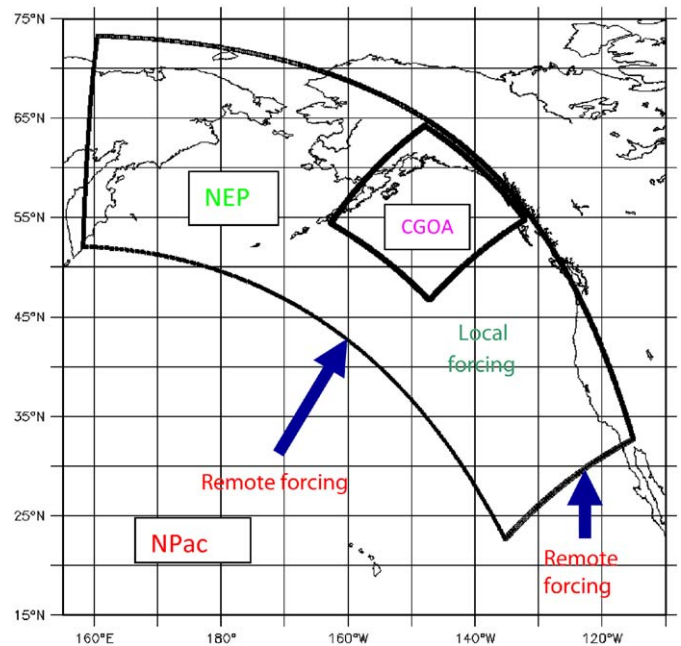

Fig. 1. Model domains and resolutions, and the definition of remote vs. local forcing used in this study. The primary focus of this paper is the NEP model with ~10-km resolution. The NPac model (20–40-km resolution) provides boundary conditions to the NEP; NEP provides boundary conditions to CGOA model (~3-km resolution).

reinforce or oppose the climatological circulation at both the coast and the shelf break, as these CTWs propagate poleward.

2. Methods

2.1. The dynamical model

In this and related GLOBEC modeling studies, we address the problem of horizontal boundary conditions with a series of nested grids in which the stored output from larger grids provides initial and boundary conditions for successively smaller grids (Fig. 1). The largest grid of the North Pacific has closed boundaries and a resolution of ~20–40 km (Curchitser et al., 2005). The intermediate grid of the northeast Pacific stretches from Baja to the Kamchatka Peninsula with a homogeneous resolution of ~10 km. A smaller grid focuses on the Coastal Gulf of Alaska (Dobbins et al., 2009) with a resolution of 3 km.

The NEP domain encompasses the critical features of the NEP's circulation. The West Wind Drift enters the open western boundary as a boundary condition derived from the NPac model, allowing investigation of how the basin gyres' positions are related to change on interannual timescales. The southern boundary is also open, allowing signals generated along the equator, such as during ENSO events, to propagate into the region. The dominant current systems affecting Alaska are included in their entirety; the model includes the entire Alaskan Stream, from its origin at the end of the West Wind Drift, to its entrance into the Bering Sea through passes between the Aleutian Islands. The grid is also fine enough to resolve (albeit crudely) the baroclinic Alaskan Coastal Current. A portion of the Arctic Ocean is included to drive flow through the Bering Straits. The northern boundary includes an outflow equivalent to the flux through Bering Strait; other than this, the northern and eastern edges of the NEP model are closed.

The models used for this study are based on the Regional Ocean Modeling System (ROMS) version 2.1, a hydrostatic, primitive equation, generalized sigma coordinate (s-coordinate) model. The time stepping scheme is described in Haidvogel et al. (2000). The pressure gradient discretization is the density Jacobian scheme described in Shchepetkin and McWilliams (2003). The third-order upstream bias scheme for horizontal advection (Shchepetkin and McWilliams, 1998) is used for tracers and 3D momentum. This scheme results in weak smoothing, which reduces the need for explicit horizontal diffusion and viscosity. Vertical advection of tracers is handled with a parabolic splines scheme, which allows longer time steps. Other features of ROMS are described in Haidvogel et al. (2008).

Major features of the NEP model are as follows. Vertical viscosity and diffusivity are achieved via the K-profile parameterization (KPP; Large et al., 1994). Bathymetry was derived from the ETOPO5 data set as described by Hermann et al. (2002). For the model nesting, tracer and 3-D momentum fields at the open boundaries are treated with a radiative boundary condition with adaptive nudging as described by Marchesiello et al. (2001). For the long-term hindcasts, we use data from the NCEP/NCAR Global Reanalysis Project as provided by the NOAA-CIRES Climate Diagnostics Center, Boulder, CO, USA, at their WWW site (http://www.cdc.noaa.gov/). Estimates of distributed freshwater input for the CGOA come from monthly values of runoff integrated along the entire Alaskan coast as derived by Royer (1982, pers. comm.) from snowpack, precipitation and temperature data. Additional point sources of runoff were derived from USGS river data. Further details of model construction and forcing are described in Appendix A.

2.2. Analysis of the basic state

Model results were stored as 3-d averages for subsequent analysis; this was a compromise between (1) hardware limits and (2) the need to analyze the response to mesoscale atmospheric weather events in general, and CTW propagation in particular. Subsequent to a 6-year initial spinup period using repeated 1996–2002 NCEP forcing data, a monthly mean climatology of NEP model results was calculated for 1997–2002.

For comparison with model output, data were obtained from two sources: AVISO altimeter data (http://www.aviso.oceanobs.com/) and daily coastal sea-level data from the University of Hawaii Sea Level Center (http://uhslc.soest.hawaii.edu/). Monthly climatologies and time averages were calculated for both data types over the period 1997–2002. For basic comparisons with the model we used anomalies of these series from their time means over the period 1997–2002. For comparisons between simulated and altimetric SSH, we also used monthly average anomalies relative to monthly climatology (monthly averaged SSHA).

For EOF analysis of observed vs. modeled SSHA over the NEP, we first interpolated the altimetry data and its climatology onto the NEP model grid. Sequential 3-d output was temporally binned into sequential monthly means, and spatially binned into 10^4-km^2 squares (that is, averaged over bins containing 10×10 model gridpoints). Monthly climatological values were calculated for each bin and subtracted from the series; EOFs were then calculated using the resulting SSHA. The top four modes explaining most of the variance were retained and compared. Significance of these modes was determined through an examination of the slope of the eigenvalue spectrum (that is, a graph of eigenvalue vs. mode number). Modes beyond which this curve leveled off (more specifically, where successive eigenvalues exhibited a smooth exponential decline) were considered as representing noise in the data/model series, rather than useful

signal. In addition, we applied North's "rule of thumb" (North et al., 1982), to assess the degeneracy of adjacent modes. Principal components (PCs) of these spatial modes were compared with the Multivariate El Niño Index (http://www.cdc.noaa.gov/people/klaus.wolter/MEI/). The MEI is based on six variables observed over the tropical Pacific: sea-level pressure, zonal and meridional components of the surface wind, sea-surface temperature, surface air temperature and total cloudiness fraction of the sky. Here the MEI is used as a basis to identify any spatial modes with a time evolution similar to El Niño, by calculating the correlation between the PCs and the MEI.

Model velocities were directly compared with current meter data from Shelikof Strait, between Kodiak Island and mainland Alaska. These data were obtained from three Aanderaa current meter moorings placed across the Strait (Stabeno et al., pers. comm.). Hourly velocities were filtered with a 120-point cosine-lanczos filter to remove tides and near-inertial oscillations. The resulting subtidal series were linearly interpolated in depth and across the Strait, to obtain the total downstrait flux. From the model, barotropic (depth-integrated) velocities were integrated across the strait (approximately five gridpoints), for comparison with the observed throughflow.

These throughflows were also calculated using finer-scale ocean and atmospheric models of the CGOA, to highlight the relative strengths and shortcomings of the NEP model configuration described in Section 2.1. The finer-scale ocean model is based on ROMS and spans the Coastal Gulf of Alaska at 3-km grid resolution, with boundary conditions derived from the NEP model. The atmospheric model is based on MM5 and spans the NPac, with nested atmospheric grids used to downscale from NCEP data (at 2° resolution) to the CGOA region (at 12-km resolution). Both of these models are described in Dobbins et al. (2009). As a sensitivity analysis, four different configurations were compared: (1) NEP with NCEP forcing; (2) NEP with MM5 forcing (finest atmospheric resolution is centered over the CGOA); (3) CGOA with NCEP forcing and (4) CGOA with MM5 forcing.

2.3. Remote vs. local forcing experiment

Our approach here is to probe the relative impact of local and remote forcing by selective removal of different forcing elements from the NEP model. We compare the results of model runs where hindcast daily average forcings are applied vs. runs where monthly climatological forcings are applied. Similarly, we compare runs where hindcast 3-d average boundary conditions (from the NPac model) are applied vs. runs where a monthly climatology of those conditions is applied.

Specifically, a climatological forcing file was constructed by deriving monthly averages of the following elements from the NCEP and runoff files for 1996–2003: wind velocity, air temperature, clouds, relative humidity, evaporation and coastal runoff.

Table 1
Summary of forcing experiments.

Run type	Surface/terrestrial forcing	Boundary conditions
1. "Standard"	NCEP daily hindcast Runoff monthly hindcast	NPac 3-d average hindcast
2. "Climatological"	NCEP monthly climatology Runoff monthly climatology	NPac climatology
3. "Variable surface"	NCEP daily hindcast Runoff monthly hindcast	NPac climatology
4. "Variable boundary"	NCEP monthly climatology Runoff monthly climatology	NPac 3-d average hindcast

A summary of the runs executed is shown in Table 1. The influence of local forcing is here defined as the difference between the "variable surface" and "climatological" runs, and the influence of remote forcing as the difference between the "variable boundary" and "climatological" runs:

Local forcing = run 3 − run 2

Remote forcing = run 4 − run 2

This decomposition implicitly assumes a linear interaction of surface and boundary effects. In the discussion we show that there is in fact little nonlinear interaction between the remote and local effects on CSL in these numerical experiments.

Much of the analysis centers on the coastal response to remote vs. local forcing. Note that a strictly contiguous coastline does not actually exist for the entire NEP; particularly in the CGOA, the coast is punctuated with small islands and irregular inlets. For our purposes, we choose points inshore of the major islands, but do not venture far upstream into minor inlets (Fig. 2). While the resulting "coastline" is slightly discontinuous, it serves reasonably well as an approximation for comparison with the CSL data, and runs parallel to the CTW waveguide (which lies further offshore).

3. Results

To demonstrate some general features resolved through nesting at the various grid resolutions and the smooth passage of information from the larger to the smaller model grids, a snapshot of model sea-surface salinity (SSS) is shown for October 8, 2001 (Fig. 3). Here the NPac, NEP and CGOA grid results are inset together on the same plot. Freshwater input from the Columbia River and the line source along the CGOA (the only sources included in this model; see Section A.5) are clearly evident. Both 10- and 3-km models are capable of capturing the 200-km scale eddies of the region (Ladd et al., 2007), but the 3-km model does a much better job of capturing the tendrils of coastal water drawn offshore by those eddies. Though not shown here, the NPac and NEP models also capture the observed subsurface cooling and freshening at line P in 2002, relative to earlier years (Curchitser et al., 2005; Freeland et al., 2003).

3.1. Seasonal features

Monthly climatologies obtained from the 6-year model sequence likewise exhibit many salient features of the NEP region (Fig. 4). The SSH is maximal in the CGOA during December, driven by the combined effects of strong downwelling favorable winds and coastal runoff. SSH is minimal in June, when both winds and runoff are weak (winds may even be upwelling favorable at this time (Stabeno et al., 2004)). The temperature field exhibits an expected north–south excursion, with advection of warmer waters poleward around the Alaskan subarctic gyre and cooler waters equatorward in the California Current. The salinity field reflects the strongest runoff of freshwater around the CGOA coastline in the fall (Royer, 1982). The Columbia River plume tends poleward along the coast in March, and equatorward along the coast in September, as observed by Hickey et al. (2005).
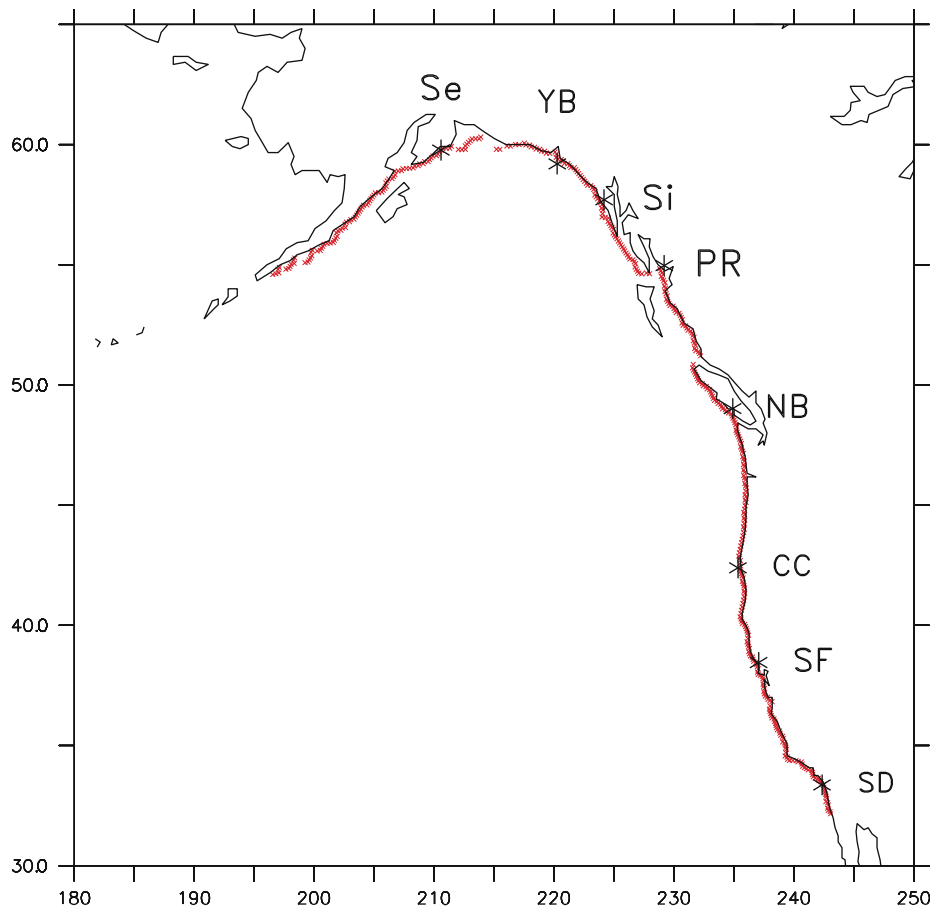

Fig. 2. Definition of the coastline for use in Hovmuller plots. Red marks indicate coastal points. Asterisks denote locations of coastal SSH data from tide gauges (SD = San Diego, SF = San Francisco, CC = Crescent City, NB = Neah Bay, PR = Prince Rupert, Si = Sitka, YB = Yakutat Bay, Se = Seward). For interpretation of the references to color in this figure legend, see the web version of this article.
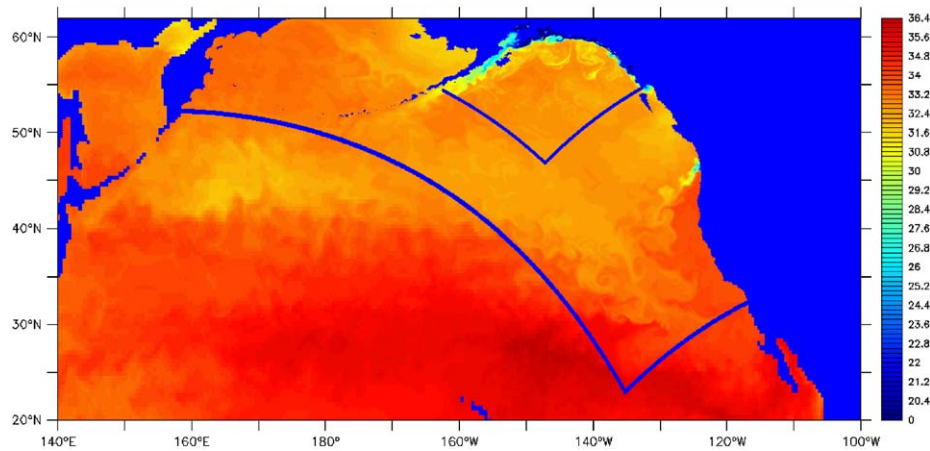
Fig. 3. Hindcast of surface salinity (psu) with nested models, for October 8, 2001. A subregion of the full basin-scale (NPac) model domain is shown. Results from regional NEP model and local CGOA model are inset. Mean horizontal grid resolution of NPac, NEP and CGOA models is approximately 30, 10 and 3 km, respectively. Note fine spatial details resolved by the CGOA model.

3.2. SSH patterns and El Niño

Here we compare snapshots of SSH from the model with AVISO altimeter data to examine the 200-km scale ("mesoscale") eddies and the evolution of the sea-surface signal during the 1997–1998 El Niño event (Fig. 5). The values shown are all anomalies about the local time mean for 1997–2002; in this manner we are attempting to create model time series equivalent to AVISO altimetry (whose mean for 1997–2002 was also removed for these plots). Monthly climatologies were not removed from the series in these plots; hence they contain both seasonal and interannual variability. During December 1997, SSH is $>5\,\mathrm{cm}$ high all along the shelf break but $>10\,\mathrm{cm}$ in the CGOA, suggesting strong local forcing of that region. During 1998, this signal gradually migrates offshore in the form of 200-km scale eddies. This progression has also been noted by Melsom et al. (1999) and Combes et al. (2009). Eddy locations are different in model and data, but a one-to-one correspondence is not expected for these mesoscale features. Eddy statistics do appear similar between the model and data; however, we have observed that in the NEP model these 200-km eddies have a shorter individual lifetime (a few months rather than 2 years sometimes observed). Longer 200-km eddy lifetimes occur in simulations with the CGOA model (not shown here). Note that these 200-km eddies are fundamentally different from shelf eddies of the Alaska Coastal Current, which are of much smaller scale.

3.3. Empirical orthogonal function analysis of monthly perturbations

The general behavior of the basic model can be further characterized using EOF analysis to compare the simulated SSHA with altimetric SSHA. Application of North's rule (North et al., 1982) indicates that the top four simulated and altimetric modes are statistically meaningful (that is, significantly different from adjacent modes); higher modes appear degenerate and are not considered further here. We begin with an examination of the altimeter data itself over an area corresponding to the model domain (Fig. 6). The first mode captures a rise (fall) in sea level in the center of the NEP (roughly at the latitude of the west wind drift), with a corresponding fall (rise) all along the coast. The PC (time series amplitude) of this mode is significantly correlated with the Multivariate El Niño Index (MEI) ($r = -.72$; if 12 degrees of freedom are assumed, this correlation has a 95% confident interval of $[-.915, -.249]$). The second mode exhibits a pronounced rise in the center of the model domain, with little

activity at the coast. A correlation of only .32 with MEI (95% confidence interval of $[-.311, .755]$) is observed for this mode. The second mode amplitude precedes the MEI in 1997; this may be associated with ENSO effects locally forced through teleconnection (Emery and Hamilton, 1985). The third mode is concentrated in a thin band near the shelf break, more closely matching the limited cross-shelf imprint of CTWs, and presumably forced by remote and local winds and runoff. A correlation of .35 with MEI (95% confidence interval of $[-.280, .769]$) is indicated, with a general correspondence of peak amplitude with peak MEI. The fourth mode is focused in a band offshore of the coast, and has the maximum amplitude of approximately 1 year following the peak MEI. As noted in Section 3.1, this is associated with eddies moving offshore after the powerful El Niño event.

After 6 years of model spinup, the EOF modes and PCs for monthly SSHA from model output are similar to those derived from the altimeter data (compare Figs. 6 and 7). The two basin-wide modes are evident, and the third and fourth mode of both model and data appear to mimic a buildup of nearshore/near-shelf sea level during the El Niño event, followed by its propagation offshore. Again, the first PC exhibits the strongest correlation with the MEI, and the fourth PC exhibits the weakest. Pointwise spatial correlations for the top four altimetric vs. simulated SSHA modes yield $r = .71, .45, .26$ and $.44$. Time correlations for the first four altimetric vs. simulated PCs yield $r = .92, .80, .64$ and $.63$. Despite the limited degrees of freedom (~100 for the spatial modes and ~12 for the PCs), these are all significantly different from zero at the 95% confidence level.

The first mode pattern in both model and data is similar to the dominant SSH mode described by Cummins et al. (2005). This mode should be associated with coherent fluctuations in pole-ward flow all along the NEP shelf break; as such, it contributes to inverse covariance in the strength of the subtropical vs. subarctic gyres as they impact the coastal region. We could think of this mode as a tilting of the West Wind Drift, such that it tends more poleward or equatorward as it approaches the coastal NEP (see Fig. 4).

3.3. Analysis of coastal sea level

Simulated CSL from the base run of the model is now compared with measured CSL from tide gauges. A Hovmuller diagram of modeled sea level along this coast is shown in Fig. 8. As in the SSH results of Fig. 5, the values shown are perturbations
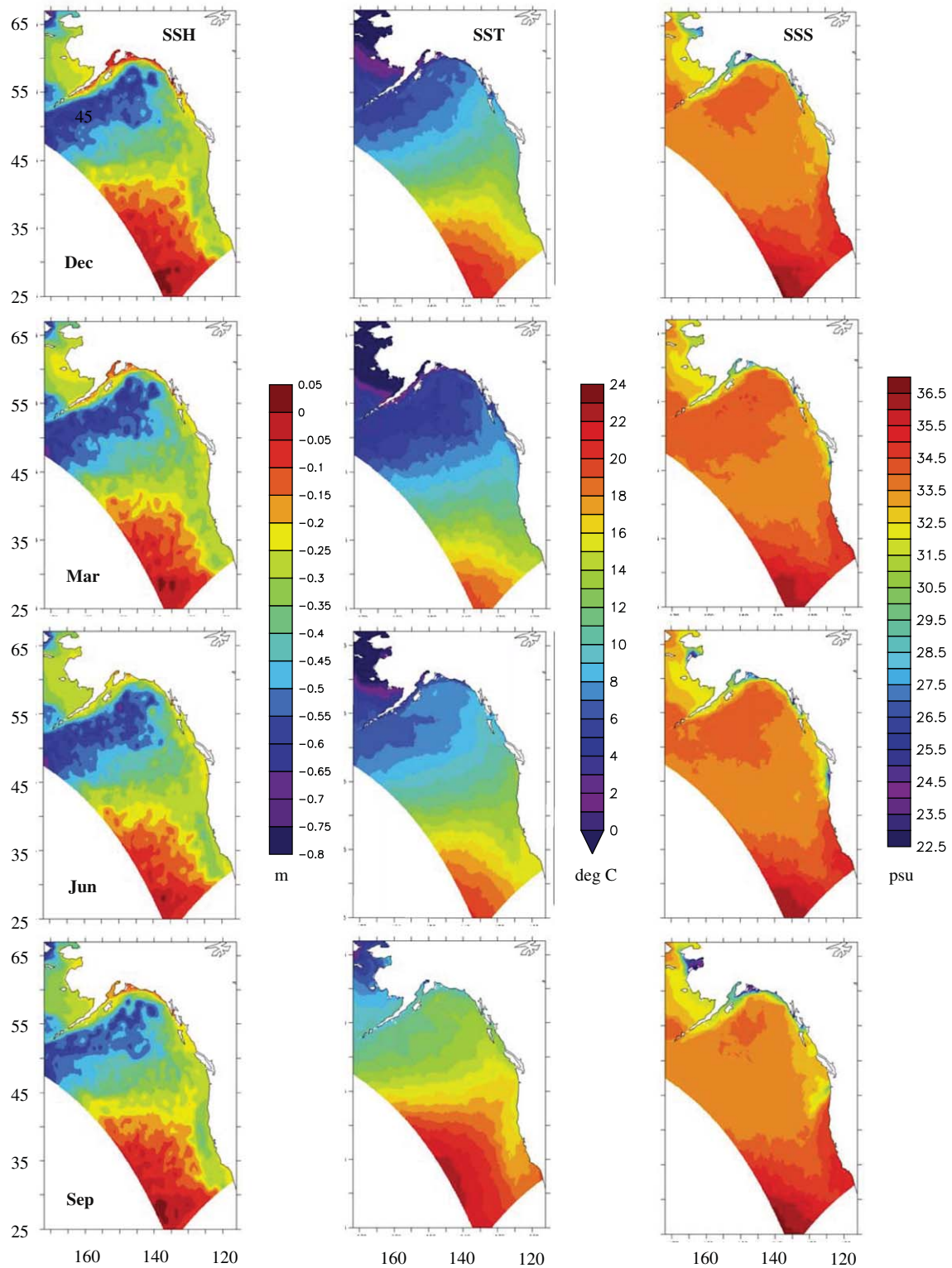
Fig. 4. Model-derived monthly climatologies for SSH (m; left), SST (°C; middle) and SSS (psu; right), for December (top), March, June and September (bottom) of 1997–2002.

from the 1997 to 2002 mean at each location. In both model and data, there is a pronounced seasonal signal to the CSL in the CGOA region, with peak values in winter. Correlations between the model-derived CSL and individual tide gauges range between .83 and .90, with the highest correspondence in the CGOA. Even if only six degrees of freedom (the number of years) are assumed, these values are all significantly different from zero at the 95%

level. The seasonal pattern to the south is weaker, with maximum values in late summer. While the model and data values are strongly correlated, the model values are significantly weaker; specifically, linear regressions at individual stations suggest the model is weaker by a factor of .31 (for California) to .47 (for the CGOA). Nonetheless in both model and data the signature of the 1997–1998 El Niño is clearly evident, with a double peak centered
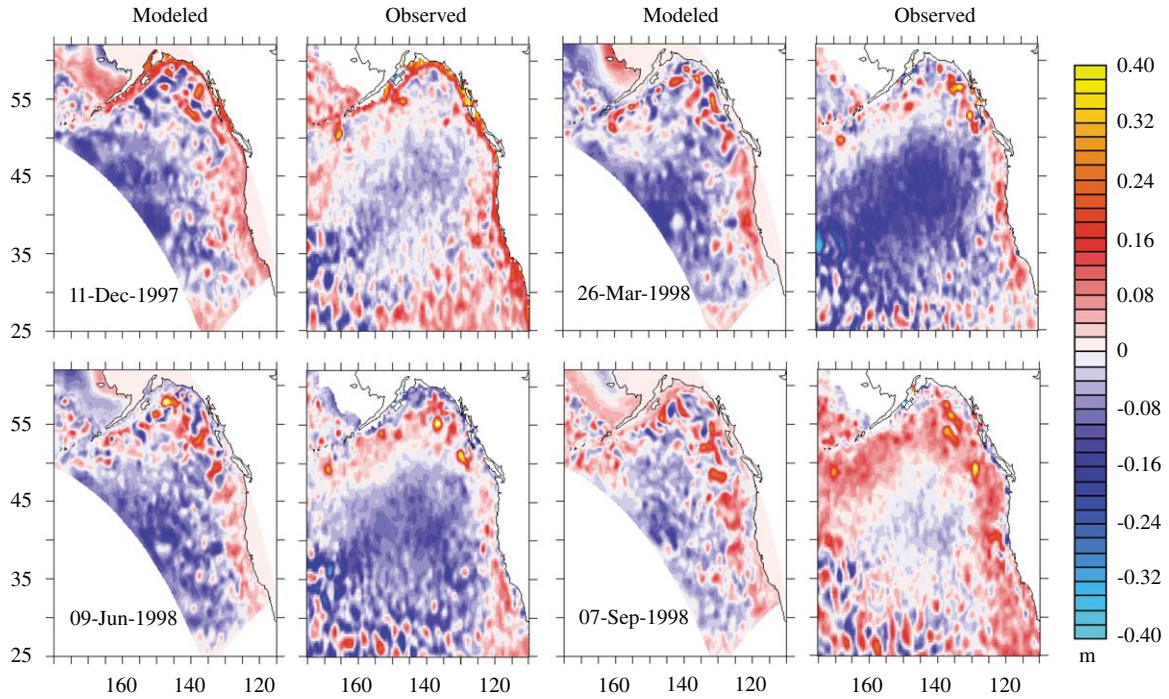
Fig. 5. Modeled and observed SSHA (cm) from 1997 to 2002 mean, for December 1997 and March, June, September 1998. In each pair of panels, the model values are on the left and the altimeter values are on the right.
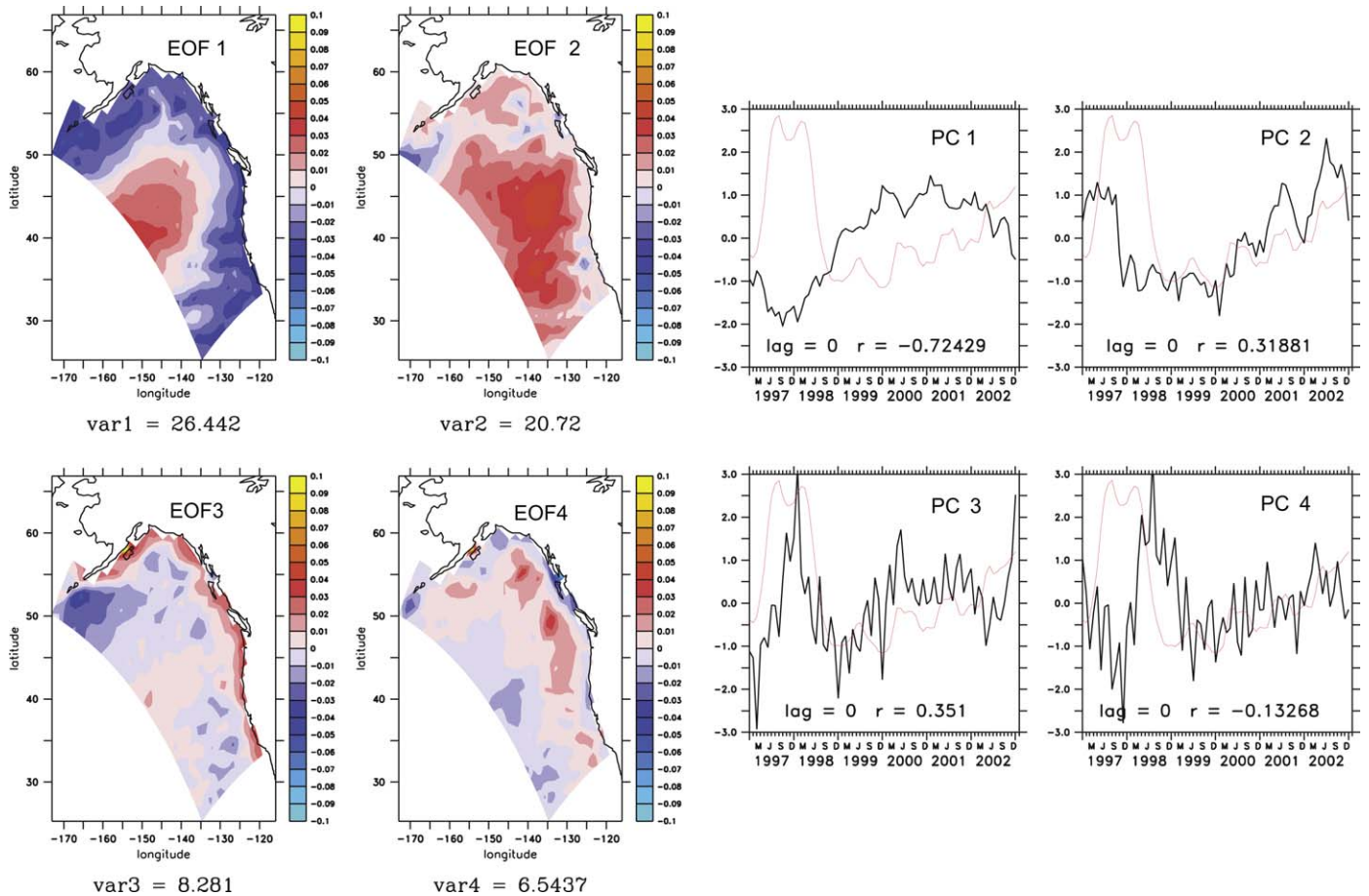

Fig. 6. EOF spatial structure and time series for the first four modes of altimeter SSHA. Percent variance explained is shown for each spatial pattern (var1–var4). The MEI index is shown as a red line for comparison with the principal component time series; correlation coefficient between principal components and MEI at zero lag is also shown.
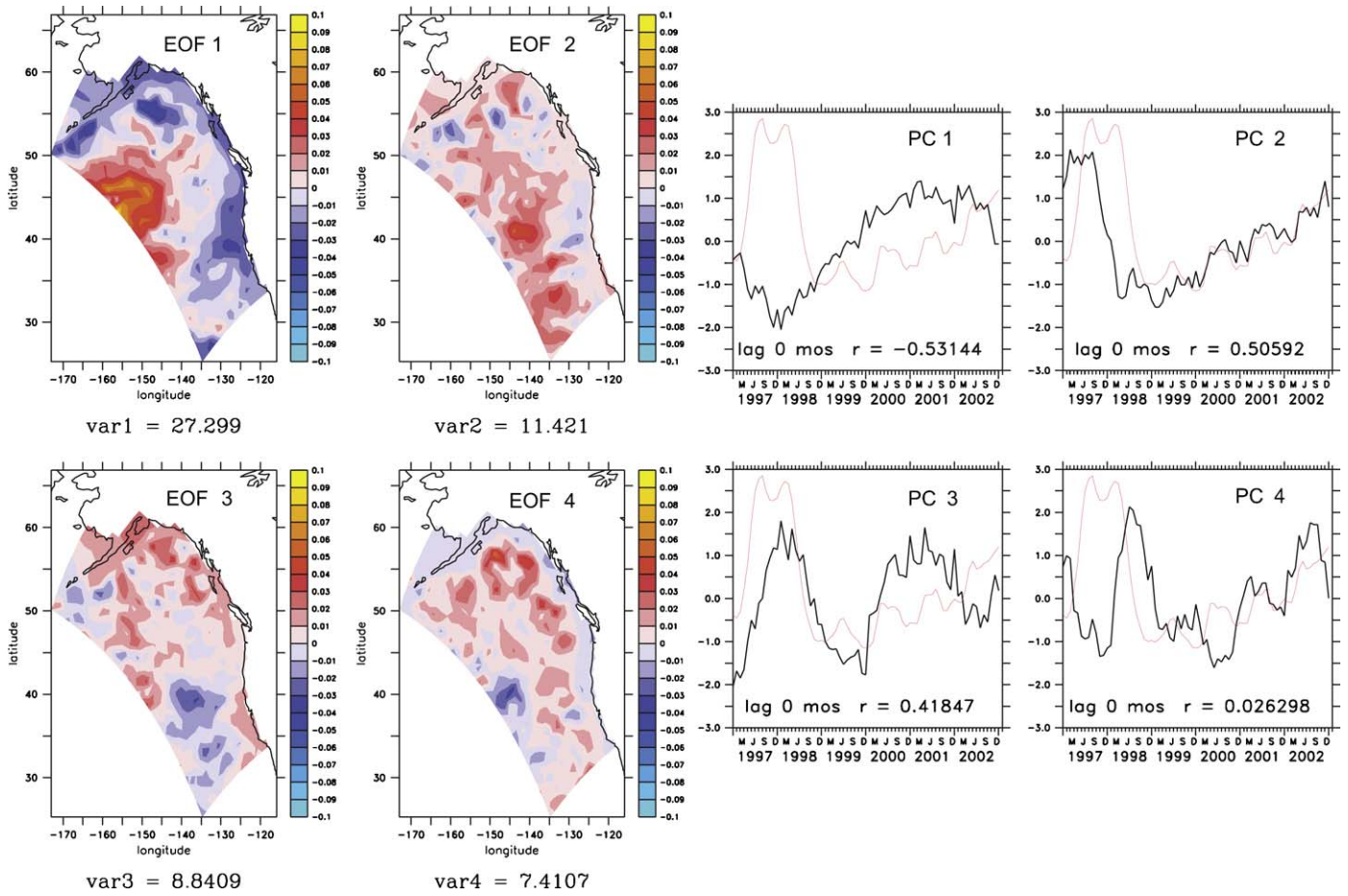
Fig. 7. As in Fig. 6, but for model SSHA. MEI index is shown as red line.
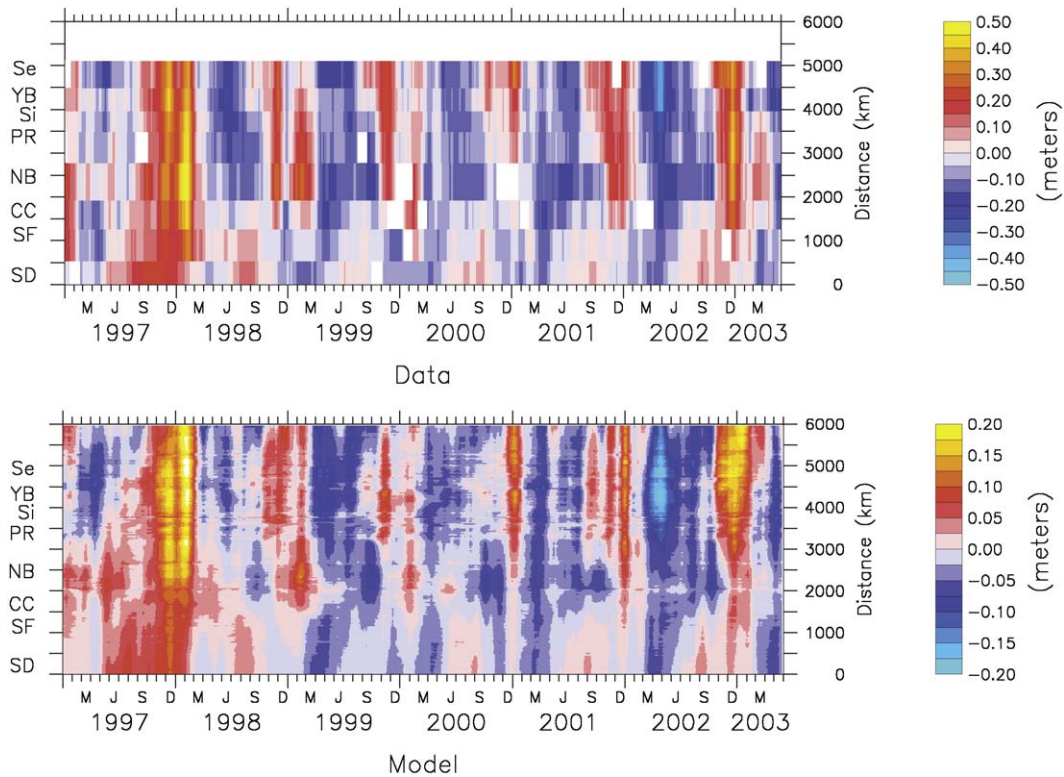

Fig. 8. Hovmuller plot of CSL (m) vs. alongshore distance for model and data. Along-coast distance (m) is shown at right. Data locations are shown at left (SD = San Diego, SF = San Francisco, CC = Crescent City, NB = Neah Bay, PR = Prince Rupert, Si = Sitka, YB = Yakutat Bay, Se = Seward).
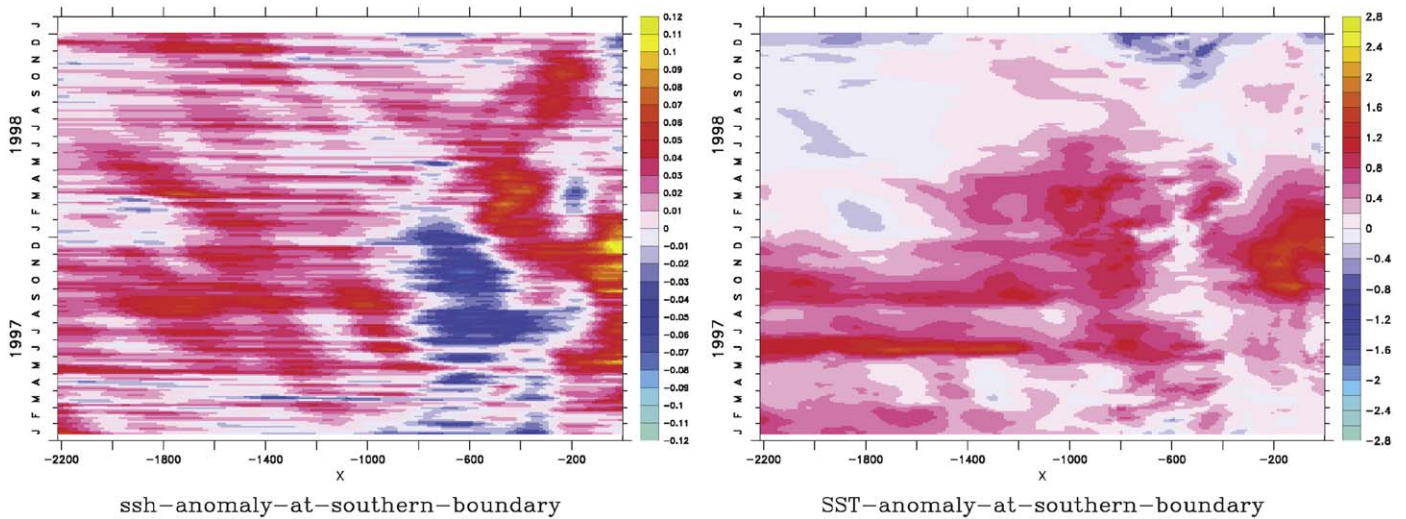
Fig. 9. Hovmuller plot of SSHA (m) and SSTA (°C) from the NPac model at the southern boundary of the NEP domain. Horizontal axis shows distance offshore (km).
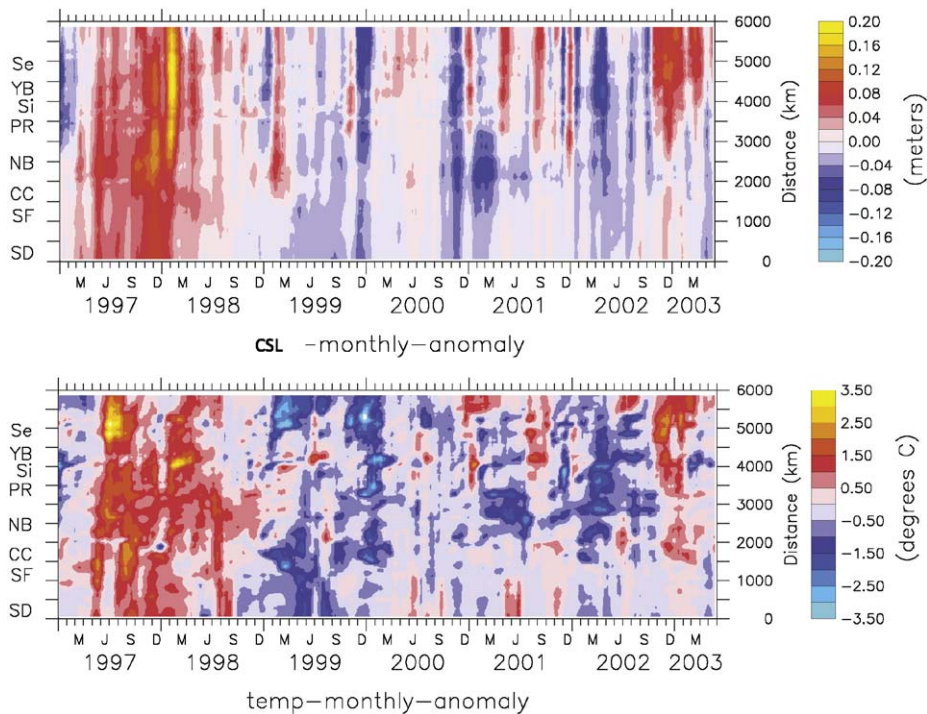

Fig. 10. Hovmuller plots of simulated monthly anomalies of CSL (m; top) and SST (°C; bottom) along the coastline. Along-coast distance (m) is shown at right. Data locations are shown at left (SD = San Diego, SF = San Francisco, CC = Crescent City, NB = Neah Bay, PR = Prince Rupert, Si = Sitka, YB = Yakutat Bay, Se = Seward).

to either side of December 1997 appearing to propagate poleward along the coast as CTWs. Curchitser et al. (2005) noted a similar propagation of a double-peaked SSH perturbation along the equator and coastline in the NPac model.

Although not the major focus of this paper, we note the regular seasonal progression of the alongshore pressure gradient south of the Alaska–British Columbia border during non-El Niño years. Roughly this corresponds to the wind-driven setup of a north–south pressure gradient (higher pressure to the north), which slackens in the spring (the "spring transition"), followed by a reversal to a south–north pressure gradient in the fall (higher pressure to the south). This alongshore pressure gradient is important in driving the coastal currents of the NEP (Hickey, 1997).

To help illustrate some characteristics of the remote forcing of the El Niño double peak in the model runs, the SSHA and SSTA for 1997–1998 (anomalies from monthly climatology) are shown for NPac output at the southern boundary of the NEP domain (Fig. 9). The coastal perturbation of SSHA is clearly evident; note that the double peak around December 1997 does not extend beyond 200-km offshore. Striations in this Hovmuller plot indicate the westward propagation of Rossby waves away from the coastline. The corresponding SSTA exhibits a strong maximum centered on December 1997, which extends ~500-km offshore.

Hovmuller plots for SSHA and SSTA (Fig. 10) help further characterize the nature of the El Niño event and its aftermath. As in Fig. 8, the tilts of the phase lines in the SSH plot are strongly suggestive of CTW propagation. The maximum SST response
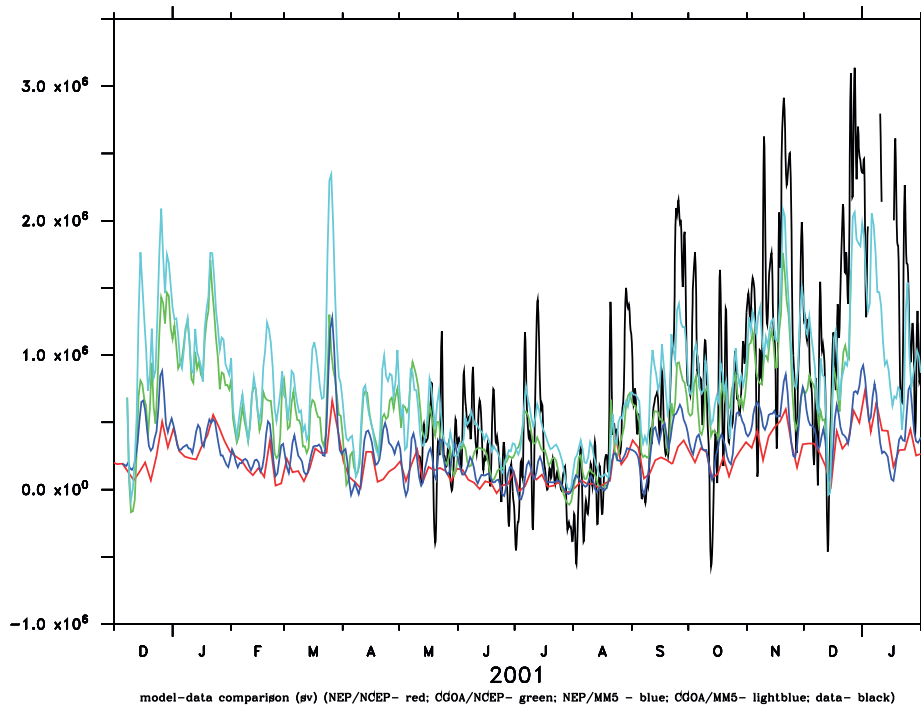
Fig. 11. Comparison of measured barotropic flux (Sv) through Shelikof Strait (black) with model estimated transports: NEP model driven by NCEP winds (red; this study); NEP model driven by fine-scale (MM5) winds (blue); CGOA model driven by NCEP winds (green; from Dobbins et al., 2009); CGOA model driven by fine-scale (MM5) winds (light blue; from Dobbins et al., 2009).
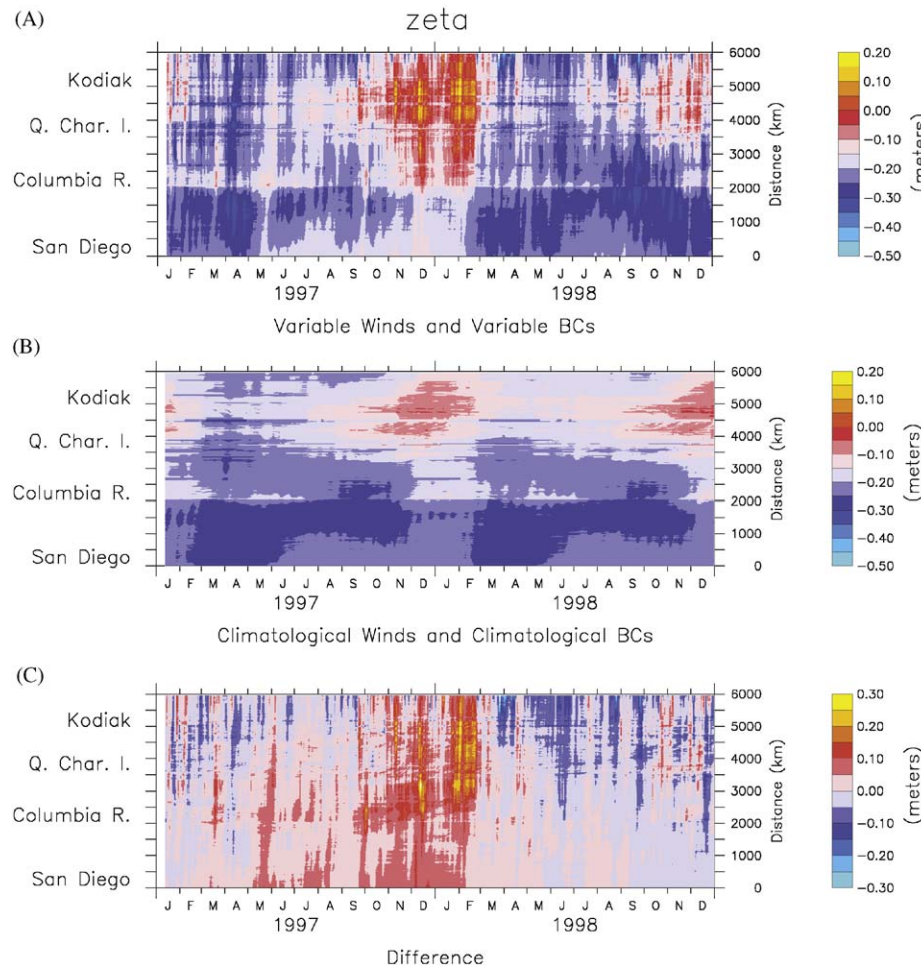

Fig. 12. Hovmuller plot of modeled coastal SSH (m) under standard hindcast (A) vs. climatological forcing and boundary conditions (B), and their difference (C).

during the strong El Niño is in the CGOA, rather than to the south. Clearly, the response to El Niño is not purely through remote forcing at the southern boundary of our domain. We attempt to quantify this more precisely in Section 3.5.

3.4. Event-scale signals in the currents

As a final metric of base model performance, the total measured barotropic flow through Shelikof Strait, obtained from a string of current meters, is compared with the corresponding flow from the NEP and CGOA models (Fig. 11). As with CSL, the NEP model driven by NCEP forcing underestimates the measured flow; nonetheless these flows are significantly correlated ($r = .74$; 95% confidence interval is [.637, .817]). The more finely resolved CGOA model, especially when driven by spatially downscaled (MM5) winds (described in Dobbins et al., 2009) exhibits a better fit with the data. For this particular metric, increasing the resolution of the ocean model appears to have a greater effect than increasing the resolution of the local atmospheric forcing.

3.5. Remote vs. local forcing experiments

Here we attempt to differentiate the local vs. remote forcing response along the coastline by selectively replacing hindcast values of boundary and forcing conditions with their monthly climatologies. The 1997–1998 base run results for simulated CSL, driven by daily hindcast forcing and boundary conditions, are

shown in Fig. 12A. Essentially this is a magnified segment of the Hovmuller diagram shown in Fig. 8. The corresponding result for climatological forcing and BCs is shown in Fig. 12B, and the difference between the two in Fig. 12C. As in Fig. 8, it is noteworthy that the largest total (local plus remote) El Niño response is found in the north (the CGOA system) and not in the south (the CC system). Apparently there is much local (or teleconnected) response, as well as that due to SSH signals at the boundary.

To quantify the remote vs. local effects, the forcing and boundary conditions are now manipulated separately as described in Section 2.3 (Fig. 13). When daily hindcast surface forcing is replaced with climatological surface forcing, CSL differences as large as .3 m emerge in the CGOA (Fig. 13A). The effect is strong north of the Columbia River, and weak to the south. A weaker signal in the south is expected (yet by no means guaranteed) a priori, insofar as wave propagation will carry the cumulative differences in wind forcing (which impact the wave characteristics all along their path) poleward along the coastal wave guide.

When the hindcast boundary conditions from the NPac model are replaced with climatological boundary conditions (Fig. 13B), a clear signal emerges of CTW propagation parallel to the coast. The perturbation wave signal is continuous up through the Aleutian Islands. While coherent CTW propagation over such a long distance is perhaps surprising given expected topographic scattering and may be partly an artifact of smoothed model bathymetry, coherent signals of this type have in fact been clearly indicated in both altimeter and tide gauge data (Meyers et al.,
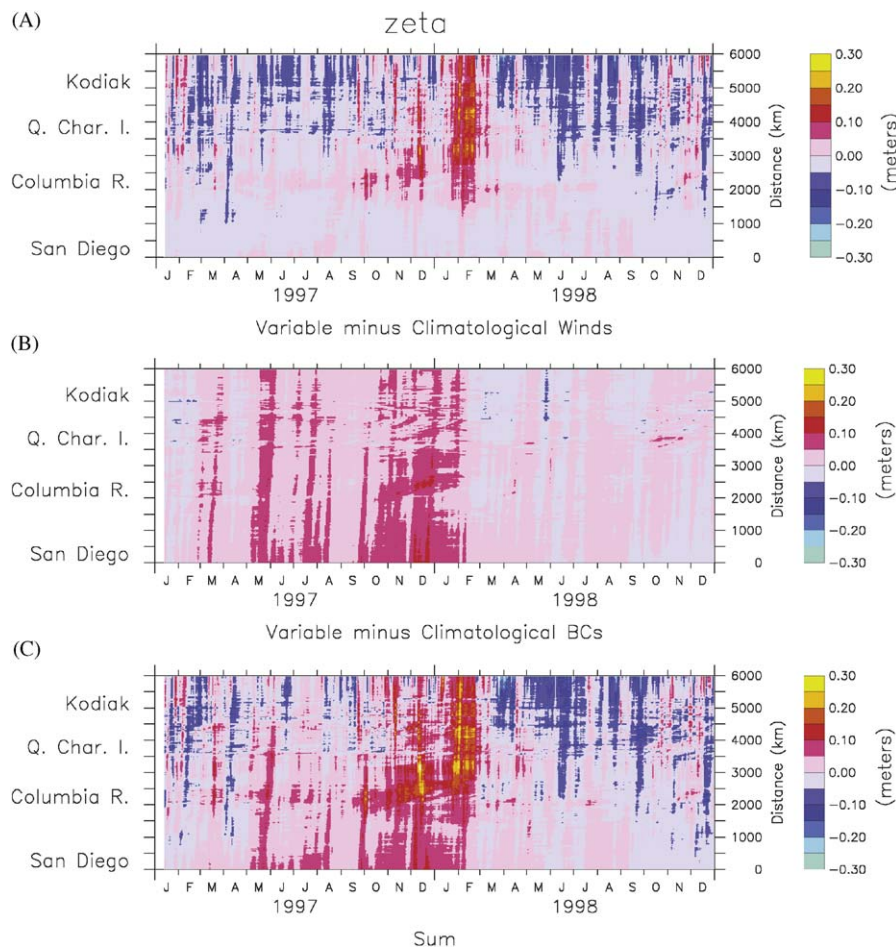

Fig. 13. Hovmuller plot of difference (m) due to variable local wind and runoff forcing vs. climatology (A), and variable boundary conditions vs. climatology (B). The sum of these results is shown in the bottom panel (C).
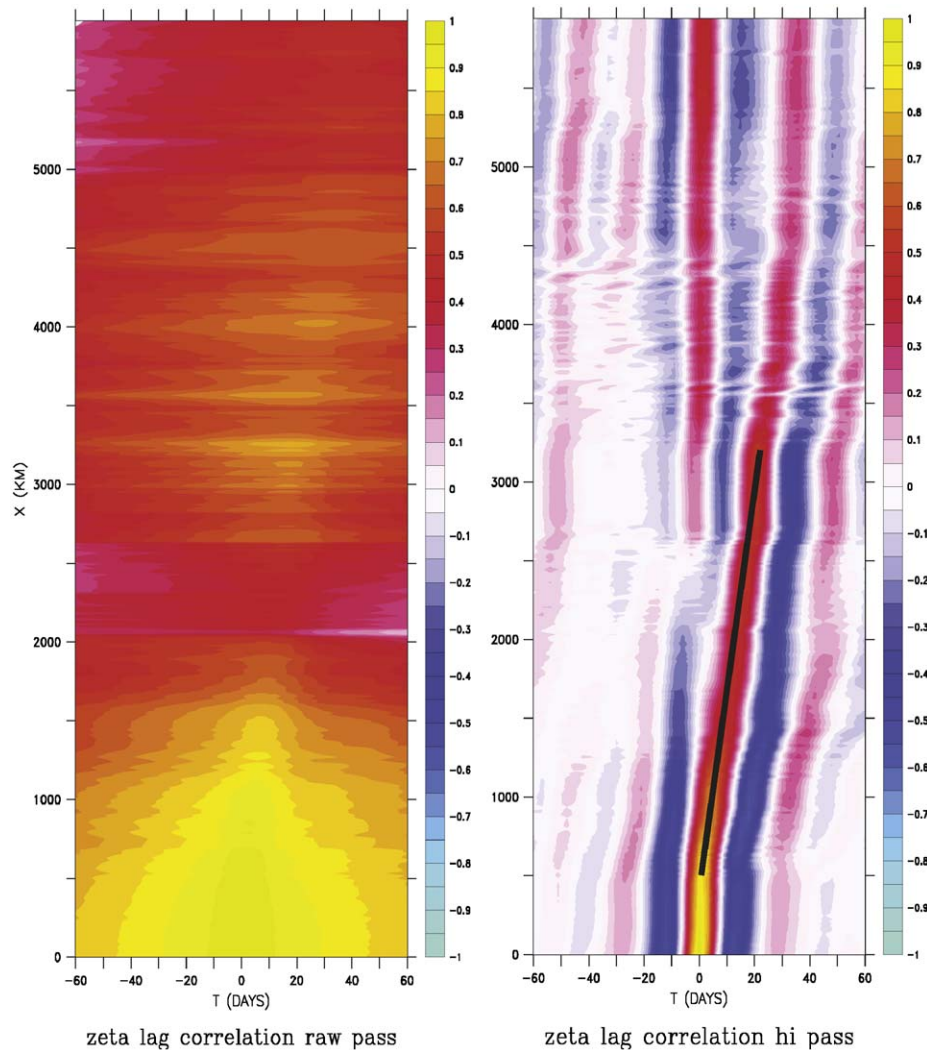
Fig. 14. Correlation between coastal points and their southern boundary value, as a function of alongshore distance and time lag. Left panel is correlation for raw values; right panel is correlation for high-passed signal (monthly and higher frequencies only). Vertical axis is along-coast distance (km); horizontal axis is time lag (d). Black line indicates mean slope of co-phase lines.

1998; Lyman and Johnson, 2008), as well as in the NPac model (Curchitser et al., 2005). The coastal signal is expected to be an underestimate of the full remotely generated CTW amplitude in the CGOA, since the shelf break is centered ~200 km from the Alaskan coast.

The sum of the residual plots from the two experiments (Fig. 13C) exhibits a close correspondence to the residual between base and purely climatological runs (Fig. 12C). This is an indication of the linearity of both local and remote impacts on CSL.

The co-phase lines in Fig. 13B suggest a wave propagation speed that we can more precisely define using lagged correlation plots. Time-lagged correlations along the coastline were calculated using raw data from the variable minus climatological BC result, and using only the high-pass filtered (monthly and higher) component of that result (Fig. 14). This analysis suggests a propagation speed of ~150 km d^{-1} for the remotely forced waves. This value falls in the middle of the range of data-based estimates calculated by several other researchers (Table 2). A significant correlation at zero time lag is also observed between the southern boundary and northern coastal points (Fig. 14). This may reflect a rise/fall in CSL all along the coastal boundary, driven by large-scale wind forcing.

Table 2
Values of coastal SSH propagation.

Present model value	150 km d^{-1}
Enfield and Allen (1980)	180
Chelton and Davis (1982)	40
Strub and James (2002a–c)	100–240
Meyers et al. (1998)	170–260

4. Discussion

4.1. EOFs and coastal trapped waves

While basic EOFs extract standing-wave modes, they are less effective at extracting progressive waves per se. However, low-frequency spatial patterns can be modulated via the characteristics of progressive waves, especially if the transit time of those waves across the spatial domain is much shorter than the averaging time used for the EOF analysis. In our case, an average higher CSL and shelfbreak SSH will appear during an El Niño year (and hence show up in the EOF modes), precisely because of the fast phase propagation of CTW characteristics. Information about

the SSH at the southern boundary is communicated through CTW characteristics, which are modified "locally" all along their poleward path.

EOFs also were calculated for the spatial difference maps from the hindcast vs. climatological forcing experiments. However, the spatial patterns were found to be dominated by the small differences in eddy locations between the various runs, and the temporal PCs corresponded to simple Fourier modes ($\sin t$, $\cos t$, $\sin 2t$, $\cos 2t$). Given the constraints of our experiments, they yielded no particularly useful information, and are hence not pursued further here. A statistically meaningful spatial comparison of the forcing experiment runs over the entire NEP domain would in fact require ensemble averaging of many model realizations, due to the energetic and partially chaotic eddy field. Here we have avoided this requirement by focusing on the CSL alone. SSHA of the basin is more heavily influenced by stochastic mesoscale features, but note that such differences between single-model realizations and data do not overwhelm the correspondence of the model SSHA with observed large-scale SSHA (Figs. 5 and 6).

4.2. Covariance of the two gyres

A recent analysis of sea-level height in the NEP by Cummins and Freeland (2007) (henceforth referred to as CF07), based on ARGO data and a quasigeostrophic model, has suggested that the bulk of variation in the sea-surface height is comprised of a positively correlated ("breathing") mode, where the California Current and Alaska Current (subtropical and subarctic gyres) vary in phase. A smaller portion of the total variance is comprised of anti-correlated variation between the two gyres. In the EOF analysis reported here, we did not detect a correlated mode per se. Our most energetic mode consisted of a major perturbation in SSHA along the axis of the West Wind Drift, and a corresponding perturbation of opposite sign all along the continental shelf. This should in fact result in anti-correlated variation of the two gyres, as it promotes coherent poleward/equatorward perturbations in

velocity all along the coast. As in the CF07 study, we do not find correlated and anti-correlated modes to appear as distinct spatial EOFs; indeed, there is no a priori reason that such modes should be spatially or temporally orthogonal, as EOF decomposition requires. The PC for the anti-correlated mode in CF07's analysis has the same basic trend as the PC of our most energetic EOF mode, and of the MEI itself—that is, a peak of poleward flow in 1997–1998, followed by a reversal of sign to equatorward flow in 1999, then a return to poleward flow in 2002. This could be viewed as an anti-correlated modification of the two gyres by ENSO, through both local (teleconnection) and remote (CTW) effects. Our failure to resolve a correlated mode may be due to the limited temporal and spatial domain of our analysis, relative to that of CF07.

4.3. Subsurface signals

Although the focus of this paper has been surface signals (and SSHA and CSL in particular), strong subsurface effects are manifest during powerful El Niño events. These may propagate along the coast, and may exhibit different propagation speeds than the surface signal. Royer (2005) reported a subsurface temperature response to El Niño in the northern CGOA with a lag time of 8–10 months. If this response is attributed to remote forcing via Kelvin waves, it corresponds to a propagation speed of $40\,\mathrm{km\,d^{-1}}$. This is substantially lower than most of the values for SSHA propagation listed in Table 2. The temperature anomaly (deviation from monthly climatology) at 100 m along the southern boundary of the NEP model is shown in Fig. 15. A strong warming event within 100 km of the coastline is clearly associated with the 1997–1998 El Niño; a general propagation of warm anomalies offshore is also observed.

An EOF modal analysis of 100 m temperatures over the NEP domain yields that the top four EOF modes are statistically meaningful based on North's rule (North et al., 1982). The first and second EOF modes (not shown) contain most of their energy at higher (annual) frequencies and have little correspondence with the interannual pattern of the MEI. The third EOF mode, which
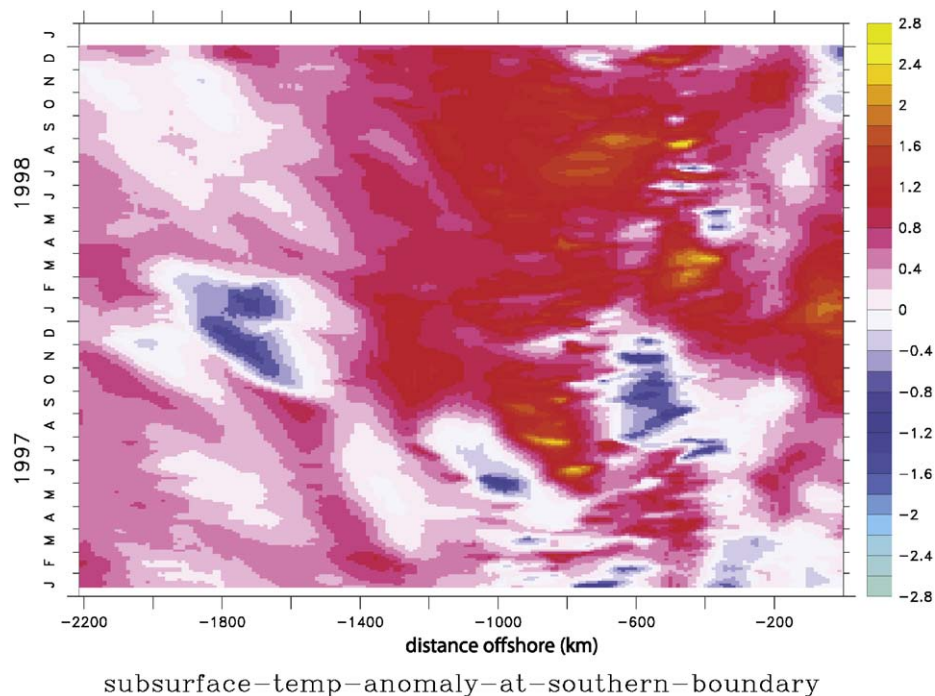

subsurface–temp–anomaly–at–southern–boundary

Fig. 15. Hovmuller plot of subsurface temperature anomalies (at 100 m depth) from the NPac model at the southern boundary of the NEP domain. Horizontal axis is marked with distance offshore.
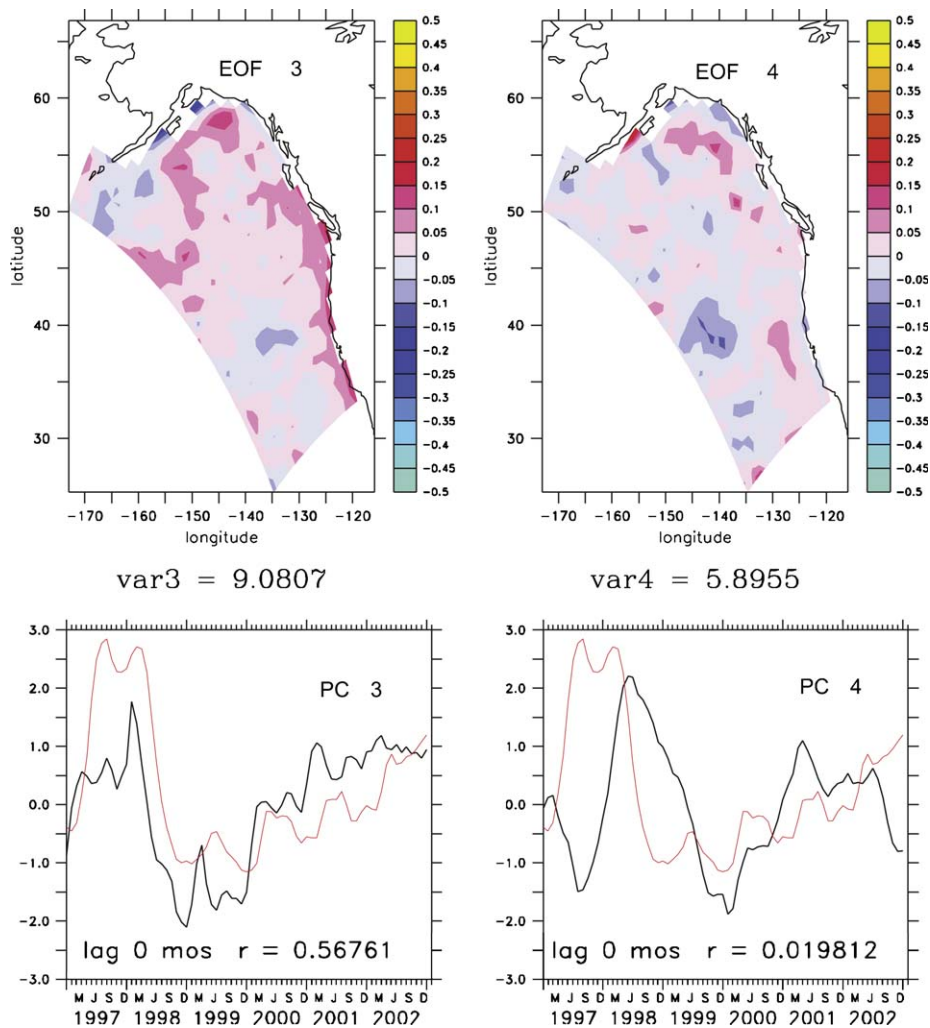
Fig. 16. EOF spatial structure and time series for subsurface temperature (100 m). Third and fourth EOF modes are shown. Percent variance explained is shown for each spatial pattern. The MEI index is shown as a red line for comparison with the principal component time series; correlation coefficient between principal components and MEI at zero lag is also shown.

explains 9% of the variance, has a coastal focus (Fig. 16). This mode is correlated with the MEI time series ($r = .56$; 95% confidence interval is [−.02, .858]), and appears to represent subsurface warming near the coast off California during the El Niño event. In the CGOA this warming is further offshore; much of the shelf is in fact shallower than 100 m in this region. The fourth spatial mode of subsurface temperature is similar in spatial structure and time amplitude to mode 4 of the SSHA analysis; it appears to reflect the offshore propagation of anticyclonic eddies (and associated depression of the thermocline), which are formed subsequent to the high sea levels produced during El Niño. Hence this mode could represent the release of potential energy stored near the shelf during the El Niño event.

4.4. Biological implications

A major focus of GLOBEC has been the possible covariance of ecosystem properties across the NEP on interannual to interdecadal time scales. It has been suggested that some properties (e.g., salmon biomass) may be inversely correlated between Californian and Alaskan waters on these time scales (Mantua et al., 1997). In the work reported here we have found interannual SSHA modes that imply anti-correlated velocity structures, simultaneously reinforcing (reducing) the subtropical gyre while

reducing (reinforcing) the subarctic gyre. During the 1997–1998 El Niño, this dynamic would tend to advect warm waters north, as observed in a subsurface mode of Fig. 16. It has been noted that the availability of subarctic zooplankton species off Oregon is associated with higher survival of ocean salmon in that region (Hooff and Peterson, 2006). If so, the results here conform to the hypothesis that coherent fluctuations in the advection of warmer/colder waters along the shelf, driven by El Niño – or the related, lower frequency fluctuations of atmospheric and oceanic conditions associated with the Pacific Decadal Oscillation (Mantua et al., 1997) – could modulate the success of salmon off the coast of Oregon. Our sensitivity study suggests that both remote and local forcing (outside of the NEP domain vs. within it) contribute substantially to this shift (see Fig. 13), to the extent that the CSL and offshore SSHA (and velocities) are related. It remains to be seen how far poleward along the shelf such biological effects will be manifest. A local biological response to increased/decreased cross-shelf (as opposed to along-shelf) transport in the CGOA is expected, based on the need of phytoplankton for both iron (more abundant on the shelf) and nitrogen (more abundant in the basin; Stabeno et al., 2004; Hinckley et al., 2009). Whether such cross-shelf fluxes are more locally or remotely driven remains an open question. Ongoing studies with 3D NPZ models (e.g., Fiechter et al., 2009; Hinckley et al., 2009; Powell et al., 2006) will help to elucidate these factors.

5. Conclusions

A regional circulation model of the northeast Pacific has been implemented for biophysical hindcasts and sensitivity studies. This model manifests many of the salient features of the NEP, including the regular seasonal progression of the alongshore pressure gradient south of the Alaska–British Columbia border during non-El Niño years, variable flow of the Alaska Coastal Current, production of 200-km eddies, and north–south advection of riverine outflows. Offshore propagation of an energetic eddy field subsequent to the 1997–1998 El Niño event is observed in both model and data.

EOF analysis of results from the NEP model, for the period 1997–2002, indicates a general correspondence of modeled sea-surface height anomaly with altimeter data. One of the dominant modes to emerge from this analysis suggests out-of-phase covariance between the subarctic and subtropical gyres. The presence of this mode is consistent with observed interannual fluctuations in the presence of subarctic zooplankton off Oregon, and the possible modulation of salmon biomass by such fluctuations. Coherent fluctuations of SSHA along the shelf are strongly correlated with El Niño, and the offshore propagation of these fluctuations subsequent to El Niño is evident in the analysis.

Our results indicate penetration of SSHA from a basin-scale model into the NEP domain (e.g., "remote influence"), with propagation as CTWs (expressed in coastal sea level) from Baja up through Alaska. Most of the CSL off Alaska in El Niño years appears due to direct forcing by local winds and runoff ("local influence"), and such anomalies (both locally and remotely forced) are much stronger than those produced off California. Subsurface temperature anomalies appear correlated with El Niño as well, and carry the signature of offshore propagating eddies subsequent to El Niño events.

Our recent GLOBEC studies have utilized an improved version of the NEP model, with atmospheric forcing and boundary conditions from the Community Climate System Model (CCSM) program. This newer version includes both ice dynamics and tides, and will further elucidate the past and expected future dynamics of the NEP region.

Acknowledgments

Appendix A. Details of NEP model construction and forcing

A.1. Model grid and bathymetry

The NEP grid has 30 vertical levels that are concentrated near the surface. For the NEP simulations, we used ROMS stretching parameters $q_S = 5$ and $q_B = .4$. The grid's topmost layer is ~ 1 m thick in the shallowest areas (30 m deep), and ~ 18 m thick over the basin (7000 m deep). The bottom topography was derived from the ETOPO5 data set as described by Hermann et al. (2002), and smoothed using a selective Shapiro filter. Between filter passes, the depth at the coastline was raised toward its initial (unsmoothed) value, to reduce the filter's impact on the shelf. Despite this precaution, the depth of the gridpoint closest to the coast ranges from 40 to 500 m, with maximum values along the steepest parts of the California coast.

A.2. Vertical mixing

Vertical viscosity and diffusivity is achieved via the K-profile parameterization (Large et al., 1994), with values of eddy viscosity and eddy diffusivity at each vertical layer set by local shear instability (a function of the gradient Richardson number), convective nonlocal transport and a surface boundary layer (a function of the bulk Richardson number, law-of-the-wall scaling, and other matching criteria). The KPP algorithm responds to changes in stratification generated at the surface by heating due to shortwave radiation (which penetrates the water column), and surface freshwater flux. We chose not to use the bottom boundary layer extension of KPP (Durski et al., 2004) since the shallowest shelf areas are not well resolved. However, the choice of bottom friction has a measurable impact on deep currents along the shelf break, such as the California Undercurrent. Use of a quadratic bottom drag coefficient of .003 (non-dimensional) produces acceptable bottom currents.

A.3. Open boundary conditions and model coupling

Tracer and 3D momentum fields at the open boundaries are treated with a radiative boundary condition with adaptive nudging as described by Marchesiello et al. (2001). Nudging timescales are 3 d for active/inflow boundary conditions, and 1 year for passive/outflow boundaries; these values allow for smooth entry of incoming signals and smooth exit of outgoing signals without excessive reflection. These fields are relaxed to boundary conditions derived from the NPac model's output. Boundary conditions for the 2D fields are treated differently to improve the exit of barotropic signals from the model domain; this different treatment is partly derived from the much faster phase and group velocities of the barotropic dynamics, compared to the baroclinic dynamics. For the free surface, we use the Chapman (1985) scheme, and for 2D momentum we use the Flather (1976) scheme. No tidal forcing was included in these simulations.

To further reduce spurious signals at the open boundaries, we employ harmonic (Laplacian) mixing in a sponge of increased horizontal diffusion and viscosity. Tracers are mixed along geopotential surfaces and momentum is mixed along constant s-coordinate surfaces. Within 10 points of the open boundaries, coefficients are ramped from their zero interior values to $500 \, \mathrm{m^2 \, s^{-1}}$ for diffusivity and $1000 \, \mathrm{m^2 \, s^{-1}}$ for viscosity. These values produced the proper damping timescale (~ 1 d for a signal 100 km in width), for removal of spurious reflections.

In the present set of experiments, initial and boundary conditions were derived from the NPac model hindcast of 1990–2003 described in Curchitser et al. (2005). The NPac hindcast was driven by daily NCEP forcing (the same forcing dataset as was used to drive the NEP base run). The NEP model was initialized at January 1996, and driven at the boundaries with 3-d averages from the NPac run. In some of the experiments, monthly climatologies of these boundary conditions were utilized, as discussed in Section 2.3.

A.4. Surface forcing

This study combines decadal hindcasts (>8 years) with the intent to track small-scale features such as eddies through their lifetime (which can be years in the Gulf of Alaska; see Ladd et al., 2007). It is therefore desirable to reduce long-term drift in tracer fields without intrusive methods that might distort instantaneous fields. One way to accomplish this is to apply atmospheric forcing fields through the use of the TOGA-COARE bulk algorithms (Fairall et al., 1996).

In this scheme, wind stress and total heat flux are calculated using both atmospheric and ocean model-generated variables. For instance, the portion of heat flux attributed to longwave radiation is calculated from air temperature, cloudiness, relative humidity and model sea-surface temperature following Berliand and Berliand (1952). Sensible heat flux is based on both air and sea temperatures; hence SST is somewhat constrained by the specified air temperature. In addition, shortwave radiation is calculated analytically, varying with location, day of year and time of day (Zillman, 1972) and corrected for cloud fraction (Laevastu, 1960) as described by Parkinson and Washington (1979). Vapor pressure's effect on shortwave radiation is derived from relative humidity and surface air temperature (Gill, 1982).

We experimented with several sets of atmospheric variables for these calculations. For the long-term hindcasts, we use data from the NCEP/NCAR Global Reanalysis Project as provided by the NOAA-CIRES Climate Diagnostics Center, Boulder, CO, USA, at their WWW site (http://www.cdc.noaa.gov/). These data have the advantage of being available on a worldwide grid for decades. There are recognized problems with these data; for example, they are known to under-represent low-lying stratus clouds, which can lead to excessive heating (Ladd and Bond, 2002). To correct for these and related factors, and to prevent spurious secular drift in the SST, we reduced the incoming solar radiation (the solar constant) in our simulations. This approach obviated the need for surface nudging of temperature, which might otherwise distort the small-scale physics. Sensitivity of the NEP and CGOA models to alternate forcing datasets is described in Dobbins et al. (2009), as well as in Sections 2.2 and 3.4 of the present work.

Freshwater enters the water column through the surface, as well as at the coastline. In our case, we estimate surface freshwater flux away from the coast with evaporation (latent heat flux) minus precipitation (rainfall rate) from the NCEP atmospheric data sets. These data have known issues but provide a consistent basis for the sensitivity tests reported here.

A.5. Terrestrial input

The dominant source of freshwater in the Gulf of Alaska is distributed runoff of precipitation, snowmelt and glacial melt via numerous tiny creeks and rivulets emanating from the steep coastal mountains. Inclusion of this line source is critical to the generation of Alaskan Coastal Current. Estimates of this freshwater input come from monthly values of runoff integrated along the entire Alaskan coast as derived by Royer (1982, pers. comm.) from snowpack, precipitation and temperature data. These data are applied equally at 229 points along the edge of the model's land mask between Ketchikan and the Kenai Peninsula. Distributed runoff from areas further south (generally, a much smaller volume than distributed runoff in the northern CGOA) is not included.

River discharge for three rivers – the Columbia, Copper and Yukon – is also included. Monthly streamflow statistics from the United States Geological Survey were acquired from the NWIS web site (http://nwis.waterdata.usgs.gov/usa/nwis/). For times

when river gauge data are not available, monthly climatological discharge is used. Temperatures of the Copper and Yukon are defined as seasonal curves based on the sea-surface temperature near the rivers' mouths. Monthly temperature for the Columbia is based on measurements by the CORIE program (http://www.ccalmr.ogi.edu/CORIE/) within the estuary. The Columbia and Yukon Rivers were input at several horizontal gridpoints because of their sizes.

Flow through the Bering Strait contributes to circulation in the Bering Sea. Long-term mean northward transport though the Bering Strait is estimated to be $.8 \times 10^6 \, \mathrm{m}^3/\mathrm{s}$ (.8 Sv) (Coachman and Aagaard, 1988). The model includes part of the Arctic Ocean, but the walls of the grid in that corner are closed. To approximate flow through an open boundary, a constant sink totaling .8 Sv is applied at 30 points along the northern wall of the model domain. The placement of this boundary far from the primary region of interest (the NEP) minimizes the artifacts associated with this "clamped" boundary condition.

Since our model does not explicitly resolve the many small estuaries of the region, there is some controversy over the best method for parameterizing their sub-gridscale influence. By mixing river water with coastal water, estuaries serve to increase the salinity of river input while increasing the total volume outflow at the surface. When such mixing is absent, there is some tendency for river outflows to produce a self-reinforcing stratification at the model's surface, in which strong stratification inhibits mixing, allowing river plumes to penetrate far into the model interior. On the other hand, rigid specification of the salinity and transport profile at the coast can yield unrealistic horizontal gradients, as the coastal signal cannot then respond to changing interior hydrography. These effects can be grid dependent, and are discussed more fully for the 3-km CGOA grid in Dobbins et al. (2009). For the NEP model, we experimented with simple profiles and compared the results with hydrographic data acquired on the Alaskan shelf (Weingartner et al., 2005) and near the Columbia River. Based on the results of these tests, we used input salinity = 0 ppt, and a transport profile that is maximum at the surface level, decreasing linearly to the bottom level. Total transport was set equal to the runoff value. We anticipate that this places estuarine dynamics further offshore than is the case in nature. However, the 10-km grid spacing of the NEP model provides an effective numerical blender for fresh coastal and saline oceanic waters, and the resulting brackish product does not appear to suffer from the self-reinforcing stratification problem noted above.

A.6. Model execution and timing

For these large modeling projects, we used the Message Passing Interface (MPI) parallelization option available in ROMS code, and the "mpich" MPI implementation. MPI is a library specification for message passing code (see http://www-unix.mcs.anl.gov/mpi/). Model runs were performed on a supercomputer of distributed parallel LINUX nodes provided by NOAA's Forecast Systems Laboratory in Boulder, CO. On 32 processors, one model year of the NEP grid took approximately 1 d of wall-clock time on this system.

References

Berliand, M.E., Berliand, T.G., 1952. Determining the net longwave radiation of the earth with consideration of the effects of cloudiness. Izvestia Akademii Nauk SSSR Seria Geofizicheskaya 1 (in Russian).

Chapman, D.C., 1985. Numerical treatment of cross-shelf open boundaries in a barotropic coastal ocean model. Journal of Physical Oceanography 15, 1060–1075.

Chelton, D.B., Davis, R.E., 1982. Monthly mean sea-level variations along the north coast of North America. Journal of Physical Oceanography 12, 757–784.

Coachman, L.K., Aagaard, K., 1988. Transports through Bering Strait: annual and interannual variability. Journal of Geophysical Research 93, 15535–15539.

Combes, V., Di Lorenzo, E., Curchister, E., 2009. Interannual and decadal variations in cross-shore mixing in the Gulf of Alaska. Journal of Physical Oceanography, in press.

Cummins, P.F., Lagerloef, G.S.E., Mitchum, G., 2005. A regional index of northeast Pacific variability based on satellite altimeter data. Geophysical Research Letters 32 (L17607), 1–4.

Cummins, P.F., Freeland, H.J., 2007. Variability of the North Pacific Current and its bifurcation. Progress in Oceanography 75 (5), 253–265.

Curchitser, E.N., Haidvogel, D.B., Hermann, A.J., Dobbins, E.L., Powell, T.M., Kaplan, A., 2005. Multi-scale modeling of the North Pacific Ocean I: assessment and analysis of simulated basin-scale variability (1996–2003). Journal of Geophysical Research 110, C11021.

Dobbins, E.L., Hermann, A.J., Stabeno, P.J., 2009. Modeled transport of freshwater from a line-source in the coastal Gulf of Alaska. Deep-Sea Research II 56 (24), 2409–2426.

Durski, S.M., Glenn, S.M., Haidvogel, D.B., 2004. Vertical mixing schemes in the coastal ocean: comparison of the level 2.5 Mellor–Yamada scheme with an enhanced version of the K profile parameterization. Journal of Geophysical Research—Oceans 109, C01015.

ECMWF, 1995. User Guide to ECMWF Products 2.1. Meteorological Bulletin M3.2. ECMWF, Reading, UK.

Emery, W.J., Hamilton, K., 1985. Atmospheric forcing of interannual variability in the Northeast Pacific Ocean: connections with El Niño. Journal of Geophysical Research 90 (C1), 857–868.

Enfield, D.B., Allen, J.S., 1980. On the structure and dynamics of monthly mean sea level anomalies along the Pacific coast of North and South America. Journal of Physical Oceanography 10, 557–578.

Fairall, C.W., Bradley, E.F., Rogers, D.P., Edson, J.B., Young, G.S., 1996. Bulk parameterization of air–sea fluxes for Tropical Ocean Global Atmosphere Coupled Ocean Response Experiment. Journal of Geophysical Research—Oceans 101, 3747–3764.

Fiechter, J., Moore, A.M., Edwards, C.A., Bruland, K.W., DiLorenzo, E., Lewis, C.V.W., Powell, T.M., Curchitser, E.N., Hedstrom, K., 2009. Modeling iron limitation of primary production in the coastal Gulf of Alaska. Deep-Sea Research II 56 (24), 2503–2519.

Flather, R.A., 1976. A tidal model of the northwest European continental shelf. Memoires de la Societe Royale des Sciences de Liege 10, 141–164.

Freeland, H., Gatien, G., Huyer, A., Smith, R., 2003. Cold halocline in the northern California Current: an invasion of subarctic water. Geophysical Research Letters 30 (3), 1141.

Gill, A.E., 1982. Atmosphere–Ocean Dynamics. Academic Press, New York, 662pp.

Haidvogel, D.B., Arango, H., Hedstrom, K., Beckmann, A., Rizzoli, P., Shchepetkin, A., 2000. Model evaluation experiments in the North Atlantic Basin: simulations in non-linear terrain-following coordinates. Dynamics of Atmosphere and Oceans 32, 239–281.

Haidvogel, D.B., Arango, H., Budgell, W.P., Cornuelle, B.D., Curchitser, E., Di Lorenzo, E., Fennel, K., Geyer, W.R., Hermann, A.J., Lanerolle, L., Levin, J., McWilliams, J.C., Miller, A.J., Moore, A.M., Powell, T.M., Shchepetkin, A.F., Sherwood, C.R., Signell, R.P., Warner, John C., Wilkin, J., 2008. Regional ocean forecasting in terrain-following coordinates: model formulation and skill assessment. Journal Computational Physics 227, 3595–3624.

Hellerman, S., Rosenstein, M., 1983. Normal monthly wind stress over the world ocean with error estimates. Journal of Physical Oceanography 13, 1093–1104.

Hermann, A.J., Haidvogel, D.B., Dobbins, E.L., Stabeno, P.J., 2002. Coupling global and regional circulation models in the coastal Gulf of Alaska. Progress in Oceanography 53, 335–367.

Hickey, B.M., Geier, S.L., Kachel, N.B., MacFadyen, A., 2005. A bi-directional river plume: the Columbia in summer. Continental Shelf Research 25, 1631–1656.

Hickey, B.M., 1997. Physical oceanography of the West Coast of North America from the Strait of Juan de Fuca to the tip of Baja California. In: Brink, K.H., Robinson, A.R. (Eds.), The Sea. Wiley, New York, pp. 345–393.

Hinckley, S., Coyle, K.O., Gibson, G., Hermann, A.J., Dobbins, E.L., 2009. A biophysical NPZ model with iron for the Gulf of Alaska: Reproducing the differences between an oceanic HNLC ecosystem and a classical northern temperate shelf ecosystem. Deep-Sea Research II 56 (24), 2520–2536.

Hooff, R.C., Peterson, W.T., 2006. Copepod biodiversity as an indicator of changes in ocean and climate conditions of the northern California current ecosystem. Limnology and Oceanography 51 (6), 2607–2620.

Johnson, M.A., O'Brien, J.J., 1990. The northeast Pacific Ocean response to the 1982–1983 El Niño. Journal of Geophysical Research 95, 7155–7166.

Ladd, C., Bond, N.A., 2002. Evaluation of the NCEP/NCAR reanalysis in the NE Pacific and the Bering Sea. Journal of Geophysical Research 107 (C10), 3158.

Ladd, C., Mordy, C.W., Kachel, N.B., Stabeno, P.J., 2007. Northern Gulf of Alaska eddies and associated anomalies. Deep-Sea Research I 54, 487–509.

Laevastu, T., 1960. Factors affecting temperature of the surface layer of the sea. Commentationes Physico-Mathematicae 25, 1.

Large, W.G., McWilliams, J.C., Doney, S.C., 1994. Oceanic vertical mixing: a review and a model with a non-local K-profile boundary layer parameterization. Reviews of Geophysics 32, 363–403.

Lyman, J.M., Johnson, G.C., 2008. Equatorial Kelvin Waves influences may reach the Bering Sea during 2002 to 2005. Geophysical Research Letters 35, L14607, doi:10.1029/2008GL034761.

Mantua, N.J., Hare, S.R., Zhang, Y., Wallace, J.M., Francis, R.C., 1997. A Pacific interdecadal climate oscillation with impacts on salmon production. Bulletin of the American Meteorological Society 78 (6), 1069–1080.

Melsom, A., Meyers, S.D., Hurlburt, H.E., Metzger, E.J., O'Brien, J.J., 1999. ENSO effects on Gulf of Alaska Eddies. Earth Interactions 3 [Available online at ⟨http://EarthInteractions.org⟩].

Marchesiello, P., McWilliams, J.C., Shchepetkin, A.F., 2001. Open boundary conditions for long-term integration of regional oceanic models. Ocean Model 3, 1–20.

Melsom, A., Metzger, E.J., Hurlburt, H.E., 2003. Impact of remote oceanic forcing on Gulf of Alaska sea levels and mesoscale circulation. Geophysical Research 108 (C11), 3346.

Meyers, S.D., Johnson, M.A., Liu, M., O'Brien, J.J., Spiesberger, J.L., 1996. Interdecadal variability in a numerical model of the northeast Pacific Ocean: 1970–89. Journal of Physical Oceanography 26, 2635–2652.

Meyers, S.D., Melsom, A., Mitchum, G.T., O'Brien, J.J., 1998. Detection of the fast Kelvin wave teleconnection due to El Niño—Southern Oscillation. Journal Geophysical Research 103 (C12), 27655–27664.

North, G.R., Bell, T.L., Cahalan, R.F., Moeng, F.J., 1982. Sampling errors in the estimation of empirical orthogonal functions. Monthly Weather Review 110, 699–706.

Pares-Sierra, A., O'Brien, J.J., 1989. The seasonal and interannual variability of the California Current System: a numerical model. Journal Geophysical Research 94, 3159–3180.

Parkinson, C.I., Washington, W.M., 1979. A large-scale numerical model of sea ice. Journal of Geophysical Research—Oceans 84, 331–337.

Powell, T.M., Lewis, C.V.W., Curchitser, E.N., Haidvogel, D.B., Hermann, A.J., Dobbins, E.L., 2006. Results from a three-dimensional, nested biological–physical model of the California Current System: comparisons with statistics from satellite imagery. Journal of Geophysical Research 111, C07018.

Royer, T.C., 1982. Coastal fresh-water discharge in the Northeast Pacific. Journal of Geophysical Research—Oceans and Atmosphere 87, 2017–2021.

Royer, T.C., 2005. Hydrographic responses at a coastal site in the northern Gulf of Alaska to seasonal and interannual forcing. Deep-Sea Research II 52, 267–288.

Shchepetkin, A.F., McWilliams, J.C., 1998. Quasi-monotone advection schemes based on explicit locally adaptive dissipation. Monthly Weather Review 126, 1541–1580.

Shchepetkin, A.F., McWilliams, J.C., 2003. A method for computing horizontal pressure-gradient force in an oceanic model with a nonaligned vertical coordinate. Journal of Geophysical Research 108 (C3), 3090.

Strub, P.T., James, C., 2002a. Altimeter-derived surface circulation in the large-scale NE Pacific Gyres: Part 1. Annual variability. Progress in Oceanography 53/2–4, 163–183.

Strub, P.T., James, C., 2002b. Altimeter-derived surface circulation in the large-scale NE Pacific Gyres: Part 2. 1997–1998 El Niño anomalies. Progress in Oceanography 53/2–4, 185–214.

Strub, P.T., James, C., 2002c. The 1997–1998 El Niño signal along the SE and NE Pacific boundaries – an altimetric view. Progress in Oceanography 54/1–4, 439–458.

Stabeno, P.J., Bond, N.A., Hermann, A.J., Kachel, N.B., Mordy, C.W., Overland, J.E., 2004. Meteorology and oceanography of the Northern Gulf of Alaska. Continental Shelf Research 24, 859–897.

Weingartner, T.J., Danielson, S.L., Royer, T.C., 2005. Freshwater variability and predictability in the Alaska Coastal Current. Deep-Sea Res. Pt. II 52, 169–191.

Zillman, J.W., 1972. A Study of Some Aspects of the Radiation and Heat Budgets of the Southern Hemisphere Oceans. Department of the Interior, Canberra, Australia, 562pp.